Pharm Res (2021) 38:1897–1914
https://doi.org/10.1007/s11095-021-03122-9

RESEARCH PAPER

Optimizing the Design of Blood–Brain Barrier-Penetrating Polymer-Lipid-Hybrid Nanoparticles for Delivering Anticancer Drugs to Glioblastoma

Taksim Ahmed[1] · Fuh-Ching Franky Liu[1] · Chungsheng He[1] · Azhar Z. Abbasi[1] · Ping Cai[1] · Andrew M. Rauth[2] · Jeffery T. Henderson[1] · Xiao Yu Wu[1]

Received: 5 July 2021 / Accepted: 7 October 2021 / Published online: 15 October 2021

© The Author(s), under exclusive licence to Springer Science+Business Media, LLC, part of Springer Nature 2021

ABSTRACT

Purpose Chemotherapy for glioblastoma multiforme (GBM) remains ineffective due to insufficient penetration of therapeutic agents across the blood–brain barrier (BBB) and into the GBM tumor. Herein, is described, the optimization of the lipid composition and fabrication conditions for a BBB- and tumor penetrating terpolymer-lipid-hybrid nanoparticle (TPLN) for delivering doxorubicin (DOX) to GBM.

Methods The composition of TPLNs was first screened using different lipids based on nanoparticle properties and *in vitro* cytotoxicity by using 2^3 full factorial experimental design. The leading DOX loaded TPLNs (DOX-TPLN) were prepared by further optimization of conditions and used to study cellular uptake mechanisms, *in vitro* cytotoxicity, three-dimensional (3D) glioma spheroid penetration, and *in vivo* biodistribution in a murine orthotopic GBM model.

Results Among various lipids studied, ethyl arachidate (EA) was found to provide excellent nanoparticle properties e.g., size, polydispersity index (PDI), zeta potential, encapsulation efficiency, drug loading, and colloidal stability, and highest anticancer efficacy for DOX-TPLN. Further optimized EA-based TPLNs were prepared with an optimal particle size (103.8 ± 33.4 nm) and PDI (0.208 ± 0.02). The resultant DOX-TPLNs showed ~ sevenfold higher efficacy than free DOX against human GBM U87-MG-RED-FLuc cells *in vitro*. The interaction between the TPLNs and the low-density lipoprotein receptors also facilitated cellular uptake, deep penetration into 3D glioma spheroids, and accumulation into the *in vivo* brain tumor regions of DOX-TPLNs.

Conclusion This work demonstrated that the TPLN system can be optimized by rational selection of lipid type, lipid content, and preparation conditions to obtain DOX-TPLN with enhanced anticancer efficacy and GBM penetration and accumulation.

KEY WORDS 3D tumor spheroids · blood–brain barrier · design of experiment (DOE) · endocytosis · glioblastoma multiforme · polymer-lipid hybrid nanoparticle

ABBREVIATIONS

3D	Three-dimensional
ABCB1	ATP-binding cassette-1
ANOVA	Analysis of variance
ApoE	Apolipoprotein E

Guest Editor: Sheng Qi

Taksim Ahmed and Fuh-Ching Franky Liu contributed equally.

Supplementary Information The online version contains supplementary material available at https://doi.org/10.1007/s11095-021-03122-9.

✉ Xiao Yu Wu
sxy.wu@utoronto.ca

[1] Advanced Pharmaceutics & Drug Delivery Laboratory, Leslie Dan Faculty of Pharmacy, University of Toronto, 144 College Street, Toronto, Ontario M5S 3M2, Canada

[2] Departments of Medical Biophysics and Radiation Oncology, Princess Margaret Cancer Centre, University of Toronto, 610 University Avenue, Toronto, Ontario M5G 2M9, Canada

BBB	Blood-brain barrier
BCRP	Breast cancer resistance protein
CDD	Central composite design
CI	Confidence intervals
CNS	Central nervous system
Cy5	Cyanine 5
DAPI	Hoechst 33,342
DL	Drug loading
DLS	Dynamic light scattering
DOE	Design of experiment
DOX	Doxorubicin
EA	Ethyl arachidate
EE	Encapsulation efficiency
EM	Ethyl myristate
EMEM	Eagle's minimum essential medium
FACS	Fluorescence activated cell sorter
FBS	Fetal bovine serum
FITC	Fluorescein isothiocyanate
FSC-A	Forward-scattering light
GBM	Glioblastoma multiforme
GM	Glycerol monostearate
HER2	Human epidermal growth receptor 2
HF 750	HiLyte Fluor ™ 750 hydrazide
HPESO	Hydrolyzed polymer of epoxidized soybean oil (HPESO)
hRAP	Human receptor-associated protein
I.V.	Intravenous
LDL-R	Low density lipoprotein receptor
MA	Myristic acid
MFI	Median fluorescence intensity
MTT	Thiazolyl blue tetrazolium bromide
M.W.	Molecular weight
NP	Nanoparticle
PCC	Pearson's correlation coefficients
PDI	Polydispersity index
PFA	Paraformaldehyde
PF68	Pluronic® F-68
P-gp	P-glycoprotein
PLN	Polymer-lipid hybrid nanoparticles;
PMAA	Poly(methacrylic acid)
poly-HEMA	Poly(2-hydroxyethyl methacrylate
PS 80	Polysorbate 80
SLN	Solid lipid nanoparticles
SA	Stearic acid
SSC-A	Side-scattered
TEM	Transmission electron microscopy
TMZ	Temozolomide
TPLN	Terpolymer-lipid nanoparticle system
VRP	Verapamil HCl

INTRODUCTION

Glioblastoma multiforme (GBM) is the most common type of malignant brain tumor among adults, accounting for ~4% of cancer-associated-deaths (1, 2). On average GBM patients survive less than 14 months after diagnosis, with only 3–5% survival at 2 years (1, 2). Unfortunately, chemotherapy and targeted therapies for brain tumors are limited due to the impermeability of most therapeutic agents across the blood–brain barrier (BBB) and progressive development of drug resistance in the central nervous system (CNS) (1, 3, 4). The BBB is characterized by the presence of tight cellular junctions which act as a highly selective permeability barrier between blood in the general circulation and the brain and spinal cord (4, 5). To achieve effective treatment outcomes, higher drug doses are typically required, leading to collateral tissue toxicity (6). For these reasons, currently, only temozolomide (TMZ) is used as the first line GBM treatment due to its good BBB permeability (7, 8). However, the loss of TMZ potency and development of tumor resistance in recurrent GBM hinder its effectiveness (7, 9, 10).

Compared to TMZ, with *in vitro* $IC_{50} > 100$ µM in U87-MG cells, doxorubicin (DOX) is more potent ($IC_{50} < 5$ µM) yet its use in GBM is restricted due to poor BBB penetration (9, 11, 12). Furthermore, DOX is a substrate of multiple efflux transporters, and thus is removed from the cells by P-glycoprotein (P-gp)/ATP-binding cassette-1 (ABCB1) and Breast Cancer Resistance Protein (BCRP/ABCG2), expressed by BBB endothelial cells (13). To increase drug delivery various methods such as pharmacological BBB disrupters, wafer implants, intracranial injection, and/or ultrasound-facilitated disruption of the BBB have been used with limited success (14). A non-invasive approach using nanoparticle (NPs) carriers that can bypass these barriers for effective drug delivery would be highly desirable.

NPs with receptor-mediated BBB-crossing capabilities have shown significant promise in drug delivery to brain tumors (3, 15–17). Compared to other BBB-targeting ligands such as antibodies, polysorbate 80 (PS 80) coated NPs offers significant advantages due to their low cost and approved use in many injectable pharmaceutical products. They deliver loaded cargo across BBB by low density lipoprotein receptor (LDL-R) mediated transcytosis by recruiting apolipoproteins (e.g., apolipoprotein E, ApoE) from plasma upon intravenous (I.V.) injection (3, 6, 18–23). However, a high concentration of PS 80 is required to achieve efficient BBB-crossing which can lead to histamine-mediated hypersensitivity syndromes in patients (24, 25). To reduce this toxicologic potential and enable

efficient drug delivery, we have devised a novel terpolymer-lipid hybrid NP (TPLN), where PS 80 is covalently bound in poly(methacrylic acid)-PS 80-grafted-starch (PMAA-PS80-St) (6, 23, 26–29). The tailorable polymer-lipid composition has enabled delivery of a variety of brain-impermeable compounds, including imaging agents (e.g. gadolinium) and small molecule anticancer drugs (e.g., DOX and docetaxel) into brain metastases of triple negative breast cancer (6, 26), and therapeutic antibody trastuzumab to brain metastases of human epidermal growth receptor 2 (HER2)-positive breast cancer (29). This versatile carrier system has significantly enhanced therapeutic efficacy in murine models of brain metastases (6).

Unlike liposomal NPs, the TPLN system is a solid monolithic matrix system (Type I polymer-lipid hybrid NP, PLN) at body temperature (30, 31). The properties of the lipid composition and content and their interactions with polymer and drugs determine the successful matrix NP formation, effective drug loading, and controllable drug release, has only been studied by limited number of groups (31–40). By rational selection of the lipid-polymer pair, a PLN can be designed to overcome cellular barriers and facilitate intracellular delivery (30, 31, 36). A PLN made of myristic acid, not stearic acid or ethyl arachidate, and hydrolyzed polymer of epoxidized soybean oil (HPESO) exhibited transformation from spherical larger particles to spiky smaller particles. This transformability enabled deeper tumor tissue penetration, enhanced cellular uptake, lipid mediated intracellular trafficking of loaded DOX in breast cancer cells in an orthotopic breast tumor (36). For a selected lipid-polymer pair, other formulation compositions may be optimized to achieve desirable particle properties and maximum drug loading efficiency. For example, the composition of verapamil HCl (VRP) loaded PLN, e.g. drug to lipid ratio and concentration of surfactant Tween®80 and Pluronic®F68, was optimized using a three-factor second order central composite design (CDD) of experiments and artificial neural networks (41). Similarly, physicochemical properties and fabrication conditions can be optimized by using the design of experiment (DOE) method (39, 42–45).

The physicochemical properties of PLNs such as particle size, surface charge (zeta potential), shape, PDI, drug loading (DL) and encapsulation efficiency (EE) are major determinants of the action of NPs in biological systems (36, 46, 47). The NPs may exhibit different velocities, diffusion characteristics, adhesion properties, *in vivo* transport, and deep tumor penetration depending on their size and shape (36, 48–54). The successful synthesis of safe, stable and effective monodispersed PLNs depends on the composition of NPs and selection of surfactants and solvents during synthesis (55). In addition, the major physicochemical properties of lipids e.g., functional groups, melting points, and molecular weights (M.W.) have a substantial influence on the DL and EE (33, 35, 36).

Herein, we investigated the role of lipid type and content on the colloidal properties of TPLN required for parenteral injection and *in vitro* cytotoxicity against GBM cells. Different fatty acid/ester based lipids were studied with varying molecular structures, M.W., melting points, functional groups, and hydrophobic chain lengths. A lead lipid was identified from the preliminary screening studies based on the effect of terpolymer and lipid characteristics on particle size, polydispersity index (PDI), DL level and encapsulation efficiency (EE). Then a two-stage optimization was conducted using 2^3 full factorial experimental design. In the first screening experiment, lipid content, sonication time and mixing time were optimized by investigating their effects on particle size, PDI, DL and EE. In the second screening experiment, sonication time and mixing time were fixed, and the effect of lipid, terpolymer and DOX amounts on particle size, PDI, DL and EE was studied to obtain the final optimal DOX-TPLN formulation. The mechanism of cellular uptake of the optimized TPLNs by human GBM U87-MG-RED-FLuc cells, the intracellular distribution of DOX and TPLN, and penetration of DOX-TPLN in 3D GBM tumor spheroids was investigated *in vitro*. The accumulation of TPLNs into a human brain tumor was further examined in an experimental orthotopic GBM xenograft murine model.

MATERIALS AND METHODS

Materials

All the reagents and culture media and their suppliers are described in detail in supplementary information (SI) SI.1.1.

Preparation and Characterization of TPLN

Terpolymer was synthesized as described previously (6, 23). The TPLN formulations containing different fatty acids or oleaginous esters, i.e. myristic acid, stearic acid, ethyl myristate and glycerol monostearate, or ethyl arachidate were first screened for optimal particle size, PDI, 24 h stability (under appropriate storage conditions) and drug EE before proceeding to optimization factorial designs.

Briefly, TPLNs were prepared by melting 50 µmol of lipid at either 58 °C or 70 °C pursuant to its respective melting point, then adding 15 mg of terpolymer, 50 µL of 100 mg mL^{-1} Pluronic® F-68 (PF68) solution, and 140 µL of a DOX 12.5 mg mL^{-1} solution. The emulsion was magnetically stirred for 20 min, and subsequently ultra-sonicated using an UP100H probe ultrasonicator at 80% peak amplitude of cycle 1 (Hielscher, Ringwood, NJ, USA) for 5 min. The resultant nano-suspension was then immediately transferred to ice-cold sterile normal saline to produce a 1 mg mL^{-1} DOX-equivalent TPLN. Samples were further diluted by 1:99 with distilled deionized water (DDI) water (Millipore-Sigma, Darmstadt, Germany), and particle sizes, PDI, and zeta potential were analyzed using a Zetasizer Nano ZS instrument (Malvern Instruments, Worchester, UK). The TPLN solution (100 µL) was centrifugally filtered using EMD Millipore Ultrafree-MC 0VV 0.1 µm pore centrifugal units at 8000 *g* for 15 min for EE and DL analyses, and later analyzed spectrophotometrically at 490 nm using the following formulae:

$$\mathrm{EE}(\%) = \frac{\{\text{mass DOX added into system}\} - \{\text{mass DOX in supernatant}\}}{(\text{mass DOX added into system})} * 100\%$$

$$\mathrm{DL}(\%) = \frac{\{\text{mass DOX added to system}\} - \{\text{mass DOX in supernatant}\}}{\{\text{mass of all PLN components added into system}\}} * 100\%$$

Additionally, the physical stability of TPLN was tested by leaving the TPLN dispersions in a 5 ± 3 °C refrigerator and retesting with dynamic light scattering (DLS) for colloidal properties after 24 h.

Optimization of TPLN Composition and Fabrication Conditions Using Multifactorial Designs

At first, the type of lipid screened for the TPLNs was investigated by two consecutive optimization processes using 2^3 factorial designs: 1) optimizing lipid content, sonication time and mixing time for particle size and PDI (experiment 1, Tables I) optimizing the content of lipid, terpolymer and DOX for particle size, PDI, and encapsulation efficiency (experiment 2, Table II). The optimal sonication and mixing times of 3 min and 5 min, respectively, were subsequently used in the second experiment. TPLNs were fabricated as mentioned previously, with variations according to their respective factor engineering levels as shown in Tables I and II.

Experiments were randomized and separated into two blocks per design to compensate for potential temporal confounders, with 2 center points (denoted as 0, 0, 0) per block (4 points total for each design) to generate a precise estimate of residual error. Both experiments were conducted chronologically according to the order presented in Tables I and II, with each block completed on separate dates.

Coded factorial points were converted to natural/engineering values using the following formula, where X_H corresponds to the natural value for "+1" and X_L for "-1", and X' is the coded value of interest:

$$X = \frac{X_H - X_L}{2} X' + \frac{X_H + X_L}{2} \quad (1)$$

The optimal conditions identified in experiment 2 were then replicated three times and a student's t-test was conducted to confirm the resultant predictability of the model. Statistical analyses and experimental designs construction were completed using JMP 14 software (SAS Institute, NC, USA).

Transmission Electron Microscopy (TEM)

The morphology of TPLNs was determined using TEM imaging. Briefly, a small volume of particles (10 µL) was diluted in DDI water (1 mL) and 5 µL of the resultant TPLN solutions pipetted on the top of a carbon coated copper grid. The TPLN solution was then air dried at room temperature. TEM images were acquired using a Hitachi H7000 electron microscope (Hitachi Canada, Ltd., Mississauga, ON, Canada) with an accelerating voltage of 75 kV.

In Vitro Cytotoxicity of DOX-TPLNs in U87-MG-RED-FLuc Cells

Human GBM U87-MG-RED-FLuc cells were obtained, cultured and maintained as described in SI.1.2. For *in vitro* cytotoxicity studies, the cells were seeded at a density of 1×10^4 per well in a 96-well plate (R&D systems, Minneapolis, MN, USA) and incubated for 48 h in a humidified incubator kept at 37 °C and 5% CO_2.

The cells were then treated with DOX-TPLN or free DOX solution at 0.01, 0.1, 0.25, 5, 10, 30, and 50 µM DOX-equivalent doses. After 24 h at 37 °C the cells were washed with Eagle's minimum essential medium (EMEM) and the percent of viable cells was determined by a standard 3-(4,5-Dimethyl-2-thiazolyl)-2,5-diphenyl-2H-tetrazolium bromide (MTT) assay as described in SI.1.3. Concentrations that inhibit 50% of cell growth (IC_{50}) were interpolated from semi-log curve-stripping of the dose–response data.

Flow Cytometric Analysis of TPLN Uptake Into U87-MG-RED-FLuc Cells

First 5×10^5 cells were seeded in 6-well tissue culture plates (R&D systems, Minneapolis, MN, USA) overnight. The cells were then incubated with 50 µL of TPLN containing fluorescein isothiocyanate (FITC)-labelled terpolymer, which was synthesized using the method described previously (36). After 4 h, the cells were rinsed with phosphate-buffered saline (PBS) twice, then centrifuged at 3,900 *g* for 5 min with FACS (Fluorescence Activated Cell Sorter) buffer (0.1% sodium azide and 5% FBS in PBS). The pellet was then redispersed and fixed in 4% paraformaldehyde (PFA) in PBS for 15 min at room temperature, centrifuged again at 3,900 *g* for 5 min, redispersed in FACS buffer, and then pipetted through Falcon™ test tube cell strainers (35 µm mesh size) to reduce cell clumping. Flow cytometric analysis was performed using a BD FACSCanto II (Becton–Dickinson Corporation, Mississauga, ON, Canada) set to 10,000 events per sample, with a 530 nm filter. Data was analyzed using FlowJo 10.5.2 (FlowJo, LCC, Ashland, OR, USA).

Confocal Microscopic Examination of Intracellular Distribution of Components of TPLN

Intracellular localization of DOX and FITC-labels TPLN was examined by fluorescence confocal microscopy. Detailed experimental method and equipment are provided in the SI.1.4.

Investigation of Cellular Uptake Mechanism of TPLN in U87-MG-RED-FLuc Cells

U87-MG-RED-FLuc cells were seeded in a 96-well plates at 1×10^4 cells per well and were grown for 48 h. Cells were then washed twice with PBS. At 37 °C, cells were pretreated with 15 µM of chlorpromazine, 20 µM of cytochalasin D, or 10 µg/mL nystatin, in growth medium for 1 h, followed by the addition of FITC-labelled TPLN suspension (240 µM DOX-equivalent) into each well. At 4 °C, cells were first treated with FITC-labelled TPLN without inhibitors. After 1 h, medium was removed, and the cells were washed twice with pre-warmed PBS (37 °C). FITC fluorescence intensities were measured using the $\lambda_{excitation}/\lambda_{emission}$ settings of 480 nm /560 nm. 96-well plates were read using a SpectraMax M2 (Molecular Devices, USA) for fluorometric analyses, and an xMark™ Microplate Absorbance Spectrophotometer (Bio-Rad, USA) for colorimetric analyses.

Investigation of the Role of LDL-R in Cellular Uptake of TPLNs

U87-MG-RED-FLuc cells were seeded at a density of 1×10^4 cells per well in a 96-well clear-bottom fluorescence plates (black) (Greiner-Bio-one, Frickenhausen, Germany) in EMEM medium containing 10% FBS and were incubated overnight at 37 °C, 5% CO_2. Cells were then pre-treated with 250 µg/mL human receptor-associated protein (hRAP), an antagonist of LDL-R (28), for 1 h, followed by co-incubation with 30 µL of FITC-labelled TPLN for 1 h. Cells were then washed three times with pre-warmed PBS (37 °C) and the fluorescence intensity measured using a microplate reader using $\lambda_{excitation}/\lambda_{emission}$ set at 480 nm / 560 nm.

In Vitro Penetration Study Using the 3D Spheroids

Tumor spheroids were grown as described in SI.1.5 and incubated with free DOX and DOX-cyanine 5 (Cy5)-TPLN for 4 h with 10 µg/mL DOX equivalent dose. The spheroids were carefully collected with gentle pipetting, centrifuged at 600 *g* for 3 min washed with PBS to remove residual DOX, and fixed with 4% PFA for 15 min at room temperature. After washing, spheroids were transferred into MakTek 35 mm glass bottom confocal dishes (MatTek Corporation, Ashland, OR, USA) with PBS and imaged by confocal microscope. Whether needed, the spheroids were kept at 4 °C until confocal imaging. Confocal images were acquired with a laser scanning confocal microscope (LSCM) (Zeiss LSM 700, Carl Zeiss, Jena, Germany) with z-stack options in which images were collected progressively at a depth of 7 µm. Detectors were set to $\lambda_{excitation}/\lambda_{emission}$ settings at 410 nm/498 nm for Hoechst 33,342 (DAPI), $\lambda_{excitation}/\lambda_{emission}$ settings = 480 nm/570 nm for DOX, and $\lambda_{excitation}/\lambda_{emission}$ settings = 649 nm/666 nm for Cy5.

Orthotopic GBM Mouse Model

A primary brain tumor model was established according to the method described by Li *et al.* with minor modifications (6). Briefly, four to six-week-old SCID mice (Princes Margaret Cancer Centre, Toronto, Canada), U87-MG-RED-FLuc cells (2×10^4) in 2 µL of media were injected intracranially into the cortex (3 mm z-depth) using a stereotactic device (SAS-5100, ASI Instruments, Warren, MI, USA). Tumor growth was monitored as a function of the cell-based luciferin signal (15 mg/kg, 10 min post-intraperitoneal injection) via bioluminescent imaging over the course of a three-week growth period using an Xenogen IVIS spectrum imager (Caliper Life Sciences, Inc., Hopkinton, MA). All animal

studies were conducted according to the ethical and legal requirements of the Ontario Animals for Research Act and the Federal Canadian Council on Animal Care guidelines; and were authorized by the University Animal Care Committee of the University of Toronto.

In Vivo Biodistribution of TPLN

Near infrared dye HiLyte Fluor ™ 750 hydrazide (HF 750) labelled-TPLNs were I.V. injected (200 µL / 20 g body weight of mouse) in the lateral tail vein of tumor bearing mice (two weeks post tumor inoculation). The biodistribution of HF 750 fluorescence-labeled TPLNs were imaged at different times points with the $\lambda_{excitation}$/ $\lambda_{emission}$ = 749 nm/ 775 nm using a Xenogen IVIS spectrum imager (Caliper Life Sciences, Inc., Hopkinton, MA). At 4 h post I.V. injection, brain, liver, spleen, kidneys, heart, and lungs were excised and immediately imaged using the Xenogen IVIS system.

The statistical analysis is mentioned in SI.1.6.

RESULTS AND DISCUSSION

Effect of Lipid Component of TPLN on Nanoparticle Properties and *In Vitro* Cytotoxicity in U87-MG-RED-FLuc Cells

The lipid component of PLNs has shown substantial impact on their stability, drug release kinetics, plasma circulation time, cellular uptake, and intracellular trafficking of drug payload (30, 36). Therefore, five different lipids of various chemical structures, M.W., and melting points, namely ethyl arachidate (EA), myristic acid (MA), stearic acid (SA), ethyl myristate (EM), and glycerol monostearate (GM) (SI.2 Table I), were screened for preparing DOX-loaded TPLN with desirable particle properties, colloidal stability, and *in vitro* cytotoxicity, at equimolar amounts against GBM cells (Fig. 1). Stability of TPLNs under short-term storage condition (5 ± 3 °C) for injectables after reconstitution was assessed by variability of colloidal properties over 24 h.

As Fig. 1a shows, the type of lipid significantly influences particle size: the largest was TPLN containing SA (331 ± 28 nm), followed by TPLNs with EA (116 ± 14 nm), MA (131 ± 37 nm), and EM (119 ± 5 nm); and the smallest with GM (36 ± 13 nm). The TPLNs stored at 5 ± 3 °C for 24 h after synthesis showed a decrease in diameter e.g. SA (137 ± 131 nm, 59% decrease, p = 0.05), MA (65 ± 16 nm, 50% decrease, p = 0.02) and EM (65 ± 28 nm, 45% decrease, p = 0.06) suggesting these lipids form less stable NPs compared to EA (93 ± 21 nm, 20% decrease, p = 0.19), or GM (35 ± 11 nm, 2% decrease, p = 0.48). As shown in Fig. 1b, the PDI was the lowest for EM (0.234 ± 0.026), and highest for MA (0.518 ± 0.007). However, TPLNs made of most of the lipids (MA, SA and EM) ended up with a PDI of 1.0 at 24 h, suggesting a loss of stability and aggregate formation over time. The modest changes in PDI (0.401 ± 0.02, 13.0% increase) for EA containing TPLNs indicates that it is likely the most stable formulation. The zeta potentials (Fig. 1c) for all TPLNs were similar for 0 to 24 h ranging between -32.9 ± 0.3 mV to -40.5 ± 0.7 mV, consistent with our previous reports (6). The negative and stable surface charge of the TPLNs are likely brought about by the anionic terpolymer component e.g., -COOH functional group in PMAA at pH 7.4 (SI.2 Fig. 1) that appears to have a larger impact on the zeta potential than the lipid component. Further evaluations of EE and DL revealed that the EA showed a high loading (6.1 ± 0.2%) and highest encapsulation (97.8 ± 0.04%) of DOX compared to other lipids (Fig. 1d and e). The DL and EE values are consistent with our previous findings that showed DL around 6% (26, 34) and EE of DOX around 75–98% (26, 28, 56). Similarly, the loading content of DOX in poly(ε-caprolactone) (PCL) and linear poly(ethylene imine) (PEI) micelles (D-PCE) was 6.56% (57). In another study, DOX loaded solid lipid NPs (SLN) was prepared using different lipids e.g., palmitic acid, SA, arachidic acid and behenic acid which showed EE of between 40 to 78% (58). Likewise, a DOX loaded SLN prepared with the lipids glyceryl caprate and curdlan showed EE and DL of 67.5 ± 2.4% and 2.8 ± 0.1%, respectively (59, 60).

The *in vitro* cytotoxicity of TPLNs with different lipids was evaluated using a standard MTT assay (Fig. 1f). The IC_{50s} between formulations and against free DOX solution (at equivalent DOX concentration) are shown in the table in Fig. 1f. While other lipid-containing DOX-TPLN exhibited similar $IC_{50's}$ as free DOX, EA-containing DOX-TPLNs appeared to be the most potent with an IC_{50} of 0.37 µM DOX, which is 12.8-fold more effective than free DOX (IC_{50} 4.75).

The superior anticancer efficacy of DOX-TPLNs made of EA might be attributed to the unique properties of EA, e.g., chemical structure, melting point, and hydrophobic interactions during NPs formation and resultant particle properties. As shown in SI.2 Table I, EA-TPLNs are likely to form soft NPs due to its lower melting temperature (41.7 °C) compared to other solid lipids (excluding EM as it is a liquid lipid at room temperature). The relatively weaker crystalline structure of EA matrix is likely to enhance DL and EE and facilitate

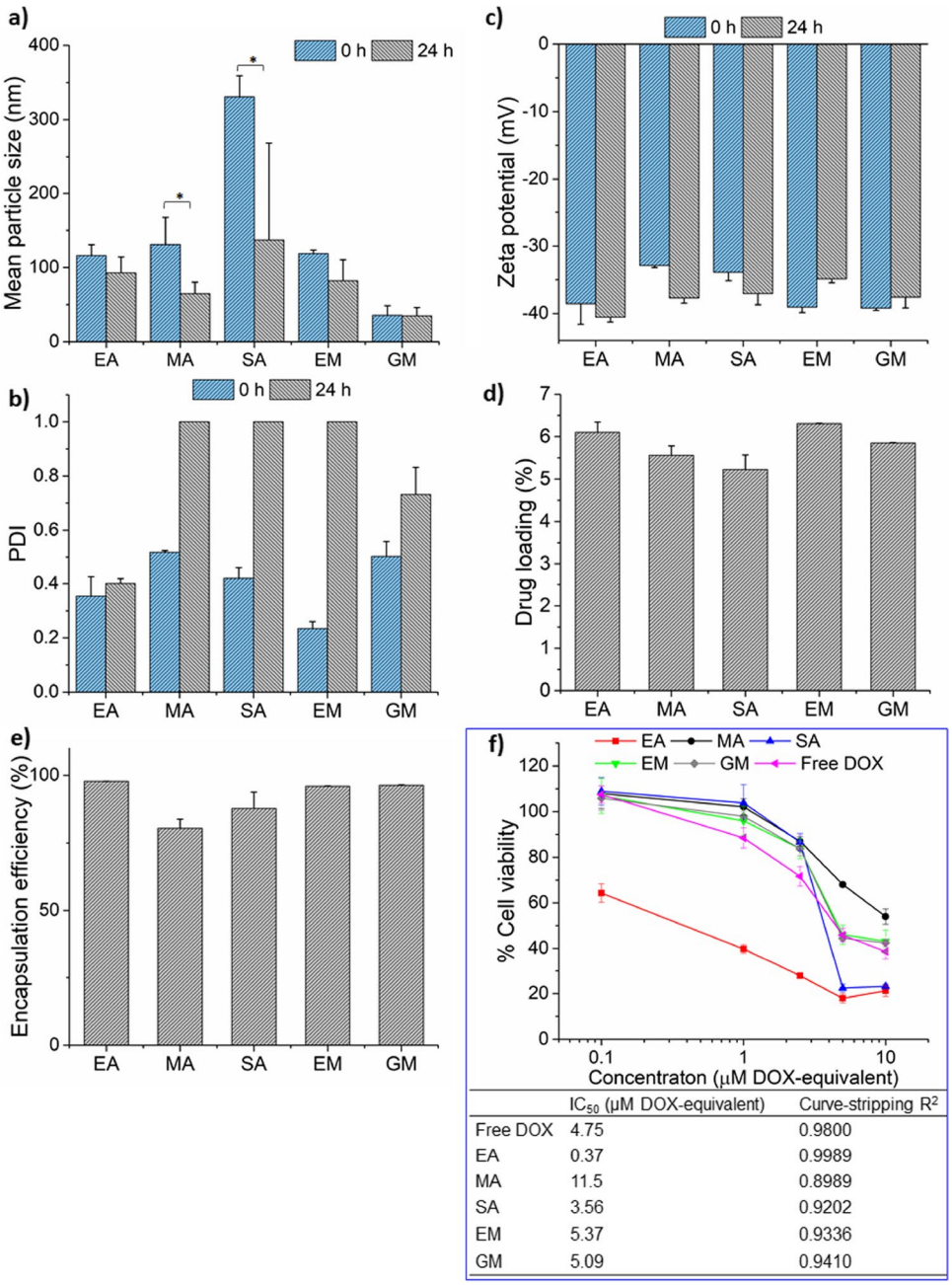

	IC_{50} (μM DOX-equivalent)	Curve-stripping R^2
Free DOX	4.75	0.9800
EA	0.37	0.9989
MA	11.5	0.8989
SA	3.56	0.9202
EM	5.37	0.9336
GM	5.09	0.9410

Fig. 1 Properties of DOX-loaded TPLNs prepared using different lipids. Mean particle size (**a**), PDI (**b**), and zeta potential (**c**) of DOX-TPLNs measured at time zero and after storage at 5±3 °C for 24 h. The drug loading content (**d**) and encapsulation efficiency (**e**) were obtained after preparing the TPLNs. **f**) *In vitro* cytotoxicity of free DOX and DOX loaded TPLNs on U87-MG-RED-Flu cells using a standard MTT assay. The data are presented as mean ± standard deviation (n=3). Table represents IC_{50} values of different treatments obtained from the cell viability curve. *P ≤ 0.05. PDI: polydispersity index; EA: Ethyl arachidate, MA: Myristic acid, SA: Stearic acid, EM: Ethyl myristate, GM: Glycerol monostearate.

higher intracellular DOX release leading to higher cytotoxicity (Fig. 1f).

Additionally, the partition of terpolymer and DOX complex into the lipid matrix may play a strong role in the cytotoxicity (36). The terpolymer consists of hydrophobic moieties, e.g., fatty chains in PS 80 and -CH2- and -CH3 groups in PMAA (SI.2 Fig. 1). After the -COOH groups in PMAA have complexed with cationic DOX via electrostatic interaction, the terpolymer becomes water-insoluble and partitions into the EA lipid droplets prior to being cooled down in a cold saline and solidifying (61). EA ($C_{22}H_{44}O_2$) (C20) has the longest aliphatic chain lengths compared to SA ($C_{18}H_{36}O_2$) (C18), GM ($C_{21}H_{42}O_4$) (C18), EM ($C_{16}H_{32}O_2$) (C14), and MA ($C_{14}H_{28}O_2$) (C14). Thus, EA could have the strongest hydrophobic interactions with hydrophobic moieties in the DOX-terpolymer and PS 80, and form more stable particles with enhanced biological activity (Fig. 1).

Taking all analyzed properties together, EA appeared to make the best TPLNs and was thus selected for subsequent studies to formulate the EA-TPLN system. In addition, EA is non-toxic to the cells even at very

high level of lipid-polymer conjugate concentrations (2.28 mM EA), as shown in SI.2 Fig. 2.

Physicochemical Characterization and Optimization of the EA-TPLN System

DOE is widely used to devise novel NPs (42, 43). It has been used to optimize SLN systems (44, 45, 62) and PS 80 coated chitosan NPs (41, 63). Thus, applying DOE to formulate TPLNs may help to design an optimized system with precise control of the physicochemical properties of the TPLN e.g., particle size, PDI, zeta potential, DL, and EE and their impact on cellular cytotoxicity.

First Factorial Design Analysis (Experiment 1)

Following the lipid screening studies, the EA-TPLN formulation was further characterized and optimized using full 2^3 factorial screening designs (experiment 1) (Fig. 2, Table I). The first screening design elucidated the impact of EA content, sonication time and mixing time on TPLNs size, PDI, zeta potential, EE and DL. Figure 2 shows a summary of the model constructed from collected data. Analysis of variance (ANOVA) shows particle size ($p=0.0167$) and PDI ($p<0.0001$) were affected by at least one of these three factors. These experiments were temporally blocked; while blocking had no effect on particle size, PDI appeared to be affected by some nuisance factor related to time of fabrication ($p<0.0001$).

Particle size appears to increase with longer mixing times ($p=0.0385$) and higher amounts of EA ($p=0.0019$), whereas PDI is decreased with high EA content ($p<0.0001$) and increased with longer sonication times ($p<0.0001$), as shown by color and asterisks in the data tables in Fig. 2. Two-factor interactions were also identified, in which increasing EA and mixing time simultaneously enhanced PDI ($p<0.0001$). Similarly increasing sonication and mixing time concurrently decrease PDI

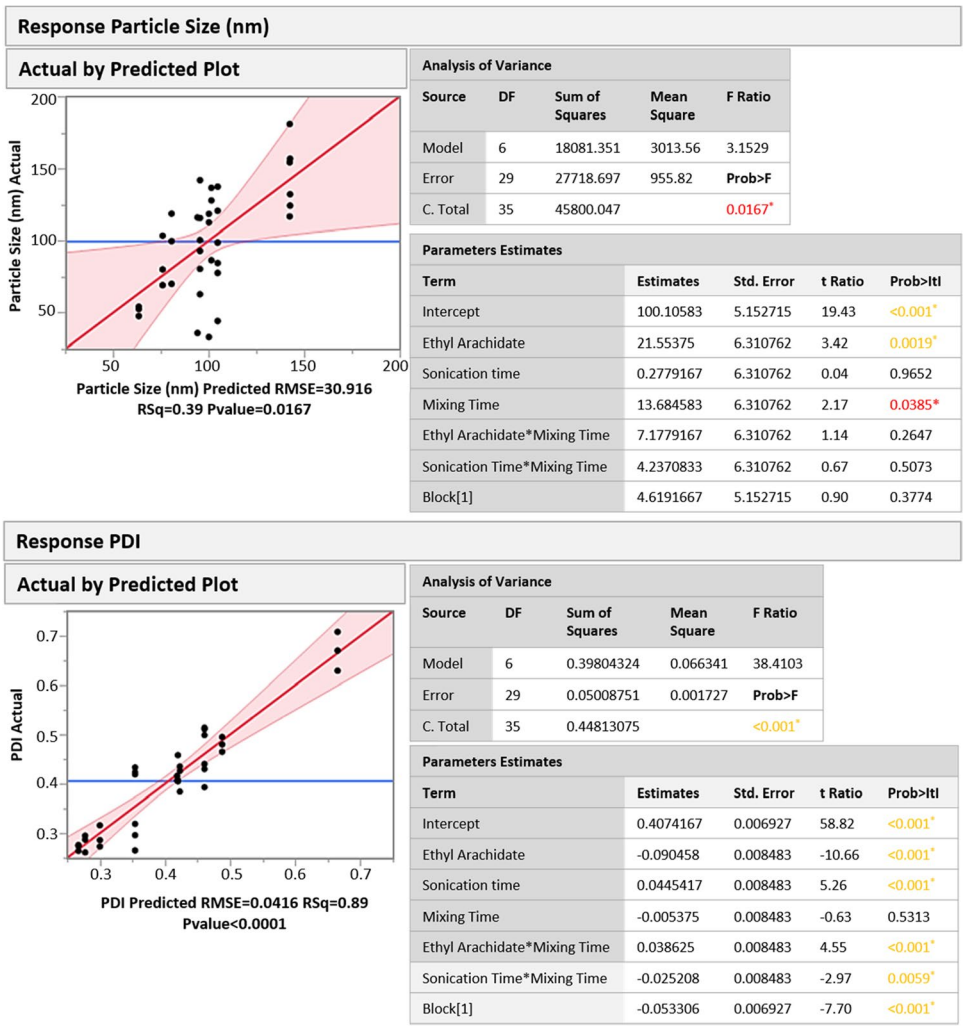

Fig. 2 Summary of model generated from a 2^3 full factorial experimental design describing effects of EA content, sonication time and mixing time on EA-TPLN formulation (experiment 1). ANOVA analysis was performed to ascertain the strength of statistical significance between factors. Model predicted values were plotted against actual values to depict residual error and linear regressions were constructed using the standard least squares method. The pink area shows the merge between the predicted and actual values based on the regression analysis. Colored and asterisked values in the tables highlight significant p-values generated from two-tailed student's t-test; in the parameter estimate charts, highlighted factors or interactions suggest that they significantly affect respective responses.

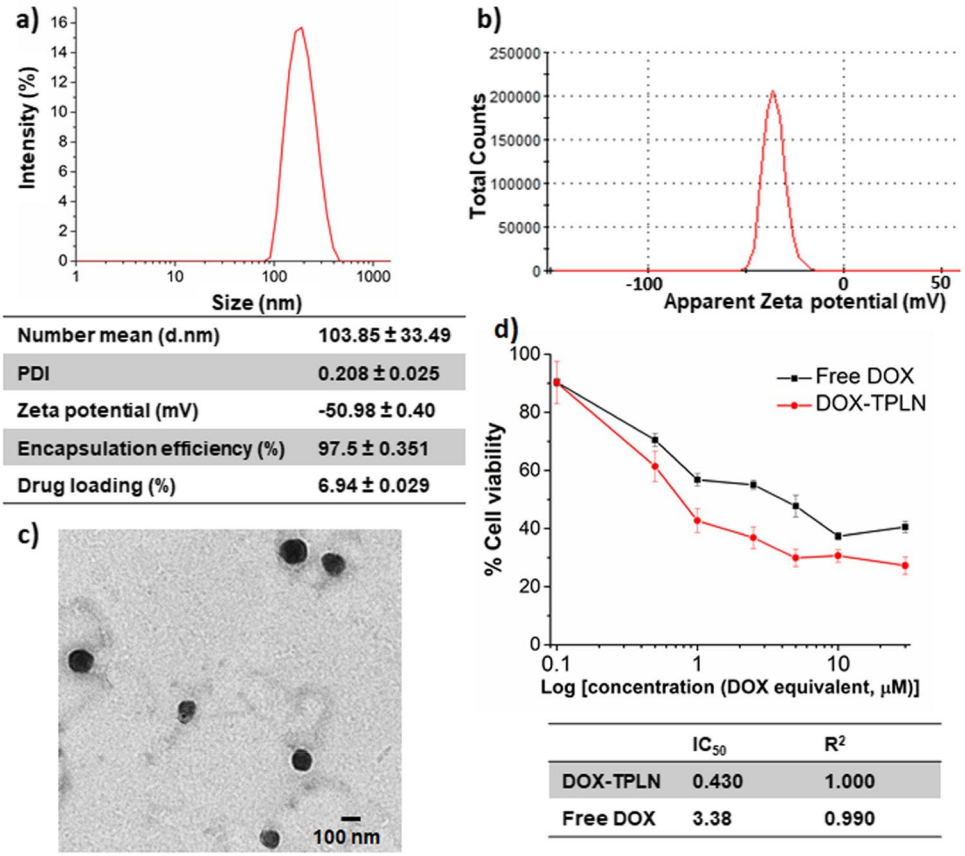

Number mean (d.nm)	103.85 ± 33.49
PDI	0.208 ± 0.025
Zeta potential (mV)	-50.98 ± 0.40
Encapsulation efficiency (%)	97.5 ± 0.351
Drug loading (%)	6.94 ± 0.029

	IC_{50}	R^2
DOX-TPLN	0.430	1.000
Free DOX	3.38	0.990

Fig. 3 Summary of TPLN physicochemical and *in vitro* properties with a representative DLS distribution plot. **a)** Representative size distribution and (**b)** zeta potential obtained using DLS for the optimized EA based TPLN formulation. **a)** Table summarizes the NPs size, PDI, zeta potential, EE and DL for TPLN. **c)** TEM images of TPLN. **d)** Cell viability of U87-MG-RED-FLuc cells treated with free DOX and DOX loaded optimized TPLN at different concentrations using a standard MTT assay. The table presents the IC_{50} calculated from the plots. The data are presented as mean ± error. Error bars represent standard error (n=3).

Table I First Experimental 2^3 Factorial Screening Design to Determine Optimal Sonication and Mixing Times

Block	Coded levels	Engineering levels		
		EA (mg)	Sonication time (min)	Mixing time (min)
1	-1, -1, -1	5	3	5
1	-1, +1, +1	5	10	15
1	0, 0, 0	10	6.5	10
1	0, 0, 0	10	6.5	10
1	+1, -1, +1	15	3	15
1	+1, +1, -1	15	10	5
2	-1, -1, +1	5	3	15
2	-1, +1, -1	5	10	5
2	0, 0, 0	10	6.5	10
2	0, 0, 0	10	6.5	10
2	+1, -1, -1	15	3	5
2	+1, +1, +1	15	10	15

Table II Second Experimental 2^3 Factorial Screening Design to Describe Effect of Lipid, Terpolymer and DOX Amount on TPLN Properties

Block	Coded levels	Engineering levels		
		EA (mg)	Terpolymer (mg)	DOX (mg)
1	+1, -1, +1	15	10	2.5
1	0, 0, 0	10	15	2.125
1	-1, +1, +1	5	20	2.5
1	0, 0, 0	10	15	2.125
1	-1, -1, -1	5	10	1.75
1	+1, +1, -1	15	20	1.75
2	+1, -1, -1	15	10	1.75
2	0, 0, 0	10	15	2.125
2	-1, -1, +1	5	10	2.5
2	-1, +1, -1	5	20	1.75
2	+1, +1, +1	15	20	2.5
2	0, 0, 0	10	15	2.125

(p=0.0059). The resultant mathematical expressions to predict various properties were:

$$Y_{Particlediameter(nm)} = 100.1 + 21.55 * x_1 + 13.68 * x_3 \quad (2)$$

$$Y_{PDI} = 0.407 - 0.090 * x_1 + 0.045 * x_2 - 0.005 * x_3 + 0.039 * x_1x_3 - 0.025x_2x_3 \quad (3)$$

where x_1, x_2, and x_3 refer to coded values (a value between -1 and 1) for the EA (mg), sonication time

(min) and mixing time (min), respectively, and $Y_{Particle\ diameter\ (nm)}$ and Y_{PDI} are predicted response values for particle diameter and PDI respectively.

The optimal conditions for the lowest particle size (101 nm) and PDI (0.246) were predicted with a desirability function generated by JMP® 14 software as shown in SI.2 Fig. 3. The optimal particles were synthesized with the shortest sonication time (coded value = -1, engineering value = 3 min) and mixing time (coded valu e = -1, engineering value = 5 min). These times were fixed in the subsequent factorial screening design; EA was studied again to determine interactions with other constituents of the EA-TPLN system.

In the first DOE analysis longer mixing times (15 min) appeared to modestly increase particle size (Fig. 2, Table III). This could be due to a longer exposure time to high temperatures, which may impact electrostatic forces between DOX and terpolymer interactions due to the added kinetic energy from heat (40, 64, 65). Furthermore, while PDI are not directly affected by mixing time, it appears that simultaneously increasing EA content and increasing mixing time broadens the particle size distribution. Adding more EA alone into the system also increases particle size. This suggests that adding EA past some saturation point will form a population of larger particles which then break down into a mixture of larger and smaller particles, potentially SLN without terpolymer as a result of the immiscibility of lipid and terpolymer (41). Furthermore, while simultaneously decreasing sonication and mixing time may synergistically reduce PDI, the magnitude of this effect is approximately half of the increase in PDI caused by longer sonication times. This emphasizes the contribution of prolonged heat exposure and its effect on PDI and that particle size/diameter outweighs the benefits of longer sonication time.

Second Factorial Design Analysis (Experiment 2)

Next, a second screening design (experiment 2) was constructed to describe the effects of the TPLN's constituents, while fixing sonication and mixing times to 3 and 5 min, respectively. SI.2 Fig. 4 and Table II show a summary of the model constructed for the second screening study. Of interest, this study showed a statistically insignificant ANOVA of particle size (p = 0.0523) and EE (p = 0.3754), somewhat contrary to the previous study shown in Fig. 2. This may be because in the first screening study, prolonged heat and mixing time were used which were reduced in the second screening study with a shorter and fixed mixing and sonication time. In the first screening study, prolonged heat and mixing time may have resulted in the formation of a bi-modal distribution of particles in which a mixture of larger and smaller particles can be found. On the other hand, it can be speculated that reducing the mixing and sonication times in second screening study may have helped in determining the changes of particle size, PDI, EE, DL upon applying different ratios of EA, terpolymer and DOX (Table IV). The lack of significance of most factor effects indicates the resiliency and robustness of the TPLN formulations to slight variations in masses of constituents.

In this study, only variations in DOX content (p = 0.0114) was found significant for PDI (ANOVA p = 0.0278). The mathematical expression to predict PDI in this system was:

$$Y_{PDI} = 0.344 + 0.055 * x_{DOX(mg)} \quad (4)$$

where $X_{DOX(mg)}$ is the amount of DOX added to the EA-TPLN system and Y_{PDI} is the predicted response values for PDI.

Because other factors were found non-significant in the range of values specified in this analysis, the

Table III Summary of Data Obtained for Analysis of First Factorial Screening Design of EA-TPLN (experiment 1) to Test Effect of EA Amount, Sonication and Mixing Time

Pattern	Particle Size (nm) Mean	PDI Mean	Zeta Potential (mV) Mean	EE (%) Mean	DL (%) Mean
– – –	96.2±24.5	0.410±0.005	-37.0±0.91	98.1±0.000	9.34±0.000
+ – –	88.2±47.7	0.271±0.006	-38.8±0.36	98.7±0.042	6.37±0.003
– + –	51.5±3.3	0.669±0.040	-39.0±0.89	98.1±0.042	9.35±0.004
– – +	84.3±17.6	0.480±0.015	-38.3±0.58	98.2±0.073	9.35±0.007
+ + –	117.0±26.8	0.292±0.022	-39.0±0.55	98.3±0.000	6.34±0.000
+ – +	137.8±17.1	0.281±0.018	-40.6±0.81	98.5±0.073	6.35±0.005
– + +	89.4±46.3	0.423±0.030	-37.5±0.86	98.1±0.042	9.34±0.004
+ + +	150.8±32.3	0.415±0.027	-35.8±0.78	97.8±0.042	6.31±0.003
0 0 0	96.5±29.1	0.412±0.082	-39.5±1.37	98.5±0.361	7.57±0.028

PDI: polydispersity index, EE: encapsulation efficiency, and DL: drug loading. Error represents the standard deviation (n=3 for each pattern)

Table IV Summary of Data Obtained for Analysis of Second Factorial Screening Design of EA-TPLN (experiment 2) to Test Effect of Ethyl Arachidate, Terpolymer and DOX Amount

Pattern	Particle Size (nm) Mean	PDI Mean	Zeta Potential (mV) Mean	EE (%) Mean	DL (%) Mean
– – –	49.4±5.1	0.441±0.015	-25.2±3.18	99.0±0.271	9.9±0.03
+ – –	67.8±34.5	0.222±0.006	-32.8±0.17	98.4±0.679	9.8±0.08
– + –	77.1±42.6	0.230±0.005	-36.6±0.87	98.8±0.073	4.6±0.00
– – +	103.7±33.4	0.362±0.021	-30.5±0.36	98.8±0.016	11.0±0.00
+ + –	118.7±8.7	0.231±0.012	-38.6±0.50	98.6±0.345	4.6±0.02
+ – +	108.7±8.5	0.369±0.010	-31.6±1.16	99.0±0.226	9.0±0.02
– + +	111.4±13.4	0.400±0.011	-33.5±0.26	98.3±1.416	9.0±0.10
+ + +	34.6±12.2	0.435±0.016	-35.9±1.18	98.6±0.117	9.0±0.01
0 0 0	92.3±44.1	0.360±0.153	-34.2±2.10	98.7±0.291	7.3±0.53

PDI: polydispersity index, EE: encapsulation efficiency, and DL: drug loading. Error represents the standard deviation (n=3 for each pattern)

desirability function, as shown in SI.2 Fig. 5, defaulted to using the least amount of material for non-significant factors. This resulted in an optimal formulation of 5 mg of EA (coded value = -1), 16.9 mg of terpolymer (coded value = 0.38) and 1.75 mg of DOX (coded value = -1) (ratio of EA: terpolymer: DOX = 1: 3.34: 0.35); this formulation, in theory, would be similar with less or more terpolymer amount (10 mg or 20 mg) as it did not significantly affect any factor of the EA-TPLN system. The predicted experimental conditions were generated irrespective of the insignificant ANOVA result for particle diameter in computing the desirability function.

This optimized formulation was replicated 9 times and two-sided Student's t-tests were performed to confirm the model's predictability and replicability of the EA-TPLN system, as shown in SI.2 Fig. 6. Non-significance between actual and predicted values of particle size ($p = 0.2048$) suggests the model sufficiently interpolates particle size values; PDI ($p = 0.0022$) and EE ($p < 0.001$), however, showed statistical significance. Upon examining 95% confidence intervals (CI) and comparing to model prediction, interval overlaps for PDI (lower CI = 0.392, upper CI = 0.542 for replicates; lower CI = 0.241, upper CI = 0.407 for model prediction) indicate that any difference between the model prediction and the replicates are very small in magnitude. A small-magnitude difference in confidence interval is also seen in EE comparisons (lower CI = 97.3%, upper CI = 97.8% for replicates; lower CI = 98.5%, upper CI = 99.2% for model prediction).

Effect of Optimized TPLNs on Nanoparticle Properties and Cytotoxicity

Upon completion of second DOE analysis, optimized EA-TPLNs were dispersed in 5% dextrose solution for I.V. administration and further studies. The optimized formulation exhibited a small PDI (Fig. 3a) and zeta potential of -35.2 (Fig. 3b). TEM images further verified the spherical shape of TPLNs (Fig. 3c). Cellular MTT analysis demonstrated a large difference in IC_{50} between free DOX and DOX-TPLN, of approximately five-fold, demonstrating improved drug delivery into U87-MG-RED-FLuc cells with the TPLN system (Fig. 3d). Differences in IC_{50} results from previous lipid screening studies (Fig. 1) may be due to increased resolution of results, as concentrations picked for MTT studies were adjusted based on the previous IC_{50} obtained. In a recent study with biomimetic NPs for glioma therapy, free DOX showed IC_{50} around 10 µg/mL (~17 µM) in U87-MG cells (66). In another study, DOX-loaded SLNs showed IC_{50} of around 1 µM on U87-MG cells (58).

Mechanisms of TPLN Uptake by Human U87-MG-RED-FLuc Cells

Next, cellular uptake of optimized EA-TPLN in U87-MG-RED-FLuc cells was investigated. Cells were incubated for 4 h and then uptake studies conducted using flow cytometry (Fig. 4a and d). Flow cytometry confirmed that the entire FITC-TPLN is taken up by U87-MG-RED-FLuc cells, as shown by statistically significant (Chi-squared $T(X) = 1682.64$, p-value < 0.001)) differences in median fluorescence intensity (MFI) between FITC-TPLNs (MFI: 1343) and control (MFI: 39.8) (Fig. 4a and b). For side-scattered (SSC-A) *vs* forward-scattering light (FSC-A) plots (Fig. 4 c and d), only cell populations with minimal variation in cell diameter were used in analyses as circled in black; the abnormally large cells (upper right) and apoptotic cells and residues (lower left) were gated accordingly between control (Fig. 4c) and treated (Fig. 4d) populations.

Endocytosis is the most common pathway by which NPs are internalized into tumor cells (67, 68). The

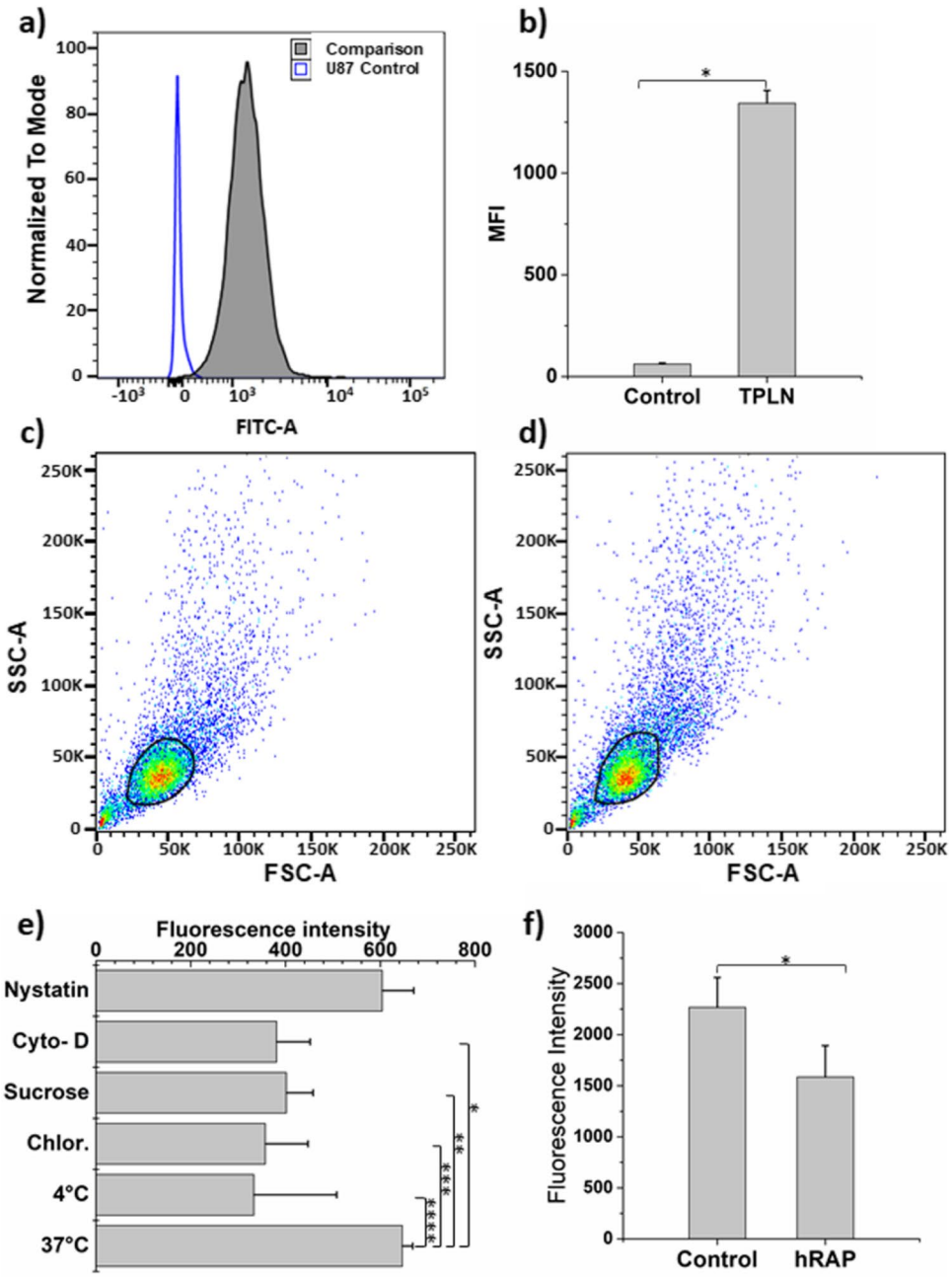

Fig. 4 Cellular uptake of FITC-TPLNs by U87-MG-RED-FLuc cells using flow cytometry (**a-d**), and study of uptake mechanism(s) of FITC-TPLNs (**e** and **f**). **a)** Representative flow cytometry analysis of shift of FITC from FITC-TPLNs upon 4 h incubation with cells, **b)** median fluorescence intensity (MFI) analysis of FITC-TPLNs compared to control. **c)** Side-scattered (SSC-A) vs **d**) forward-scattering light (FSC-A) plots where the black circled areas indicate the proportion used for subsequent analysis. **e**) Effect of incubation temperature and co-incubation with various modifiers of cellular endocytotic cycling, phagocytosis, macropinocytosis, clathrin-dependent endocytosis and caveolin-dependent endocytosis in respective order shown in the graph. **f**) Effect on cellular uptake of co-incubation with LDL-containing human serum with or without LDL-R antagonist hRAP. Data are presented as the mean ± SD (n = 3). Cyto-D: Cytochalasin D, Chlor.: Chlorpromazine.

NP size and surface chemistry play a vital role in the endocytotic uptake mechanism. The NPs smaller than 200 nm undergo clathrin-mediated endocytosis, whereas larger particles are internalized by phagocytosis (36, 67, 68). Therefore the *in vitro* cellular uptake mechanism was studied for these NPs via co-incubation of various endocytosis inhibitors with the cells (Fig. 4 e and f). Uptake of FITC-TPLNs was decreased at 4 °C, suggesting that an active transport mechanism is involved in cellular transport, and that there is low or no contribution of passive diffusion for TPLN uptake into cells. Furthermore, uptake was decreased when cells were co-incubated with cytochalasin D (inhibitor of phagocytosis), sucrose or chlorpromazine (inhibitors of clathrin-dependent endocytosis), suggesting that TPLN uptake is likely mediated by more than one process, as shown in Fig. 4e. Nystatin did not significantly affect TPLN uptake, suggesting that caveolin-dependent endocytosis may not be the major endocytotic pathway. These uptake results suggest that TPLN may be taken up via multiple endocytic pathways and imply that this TPLN system relies largely on phagocytosis, macropinocytosis and clathrin-dependent endocytosis. These observations are consistent with our previous studies in

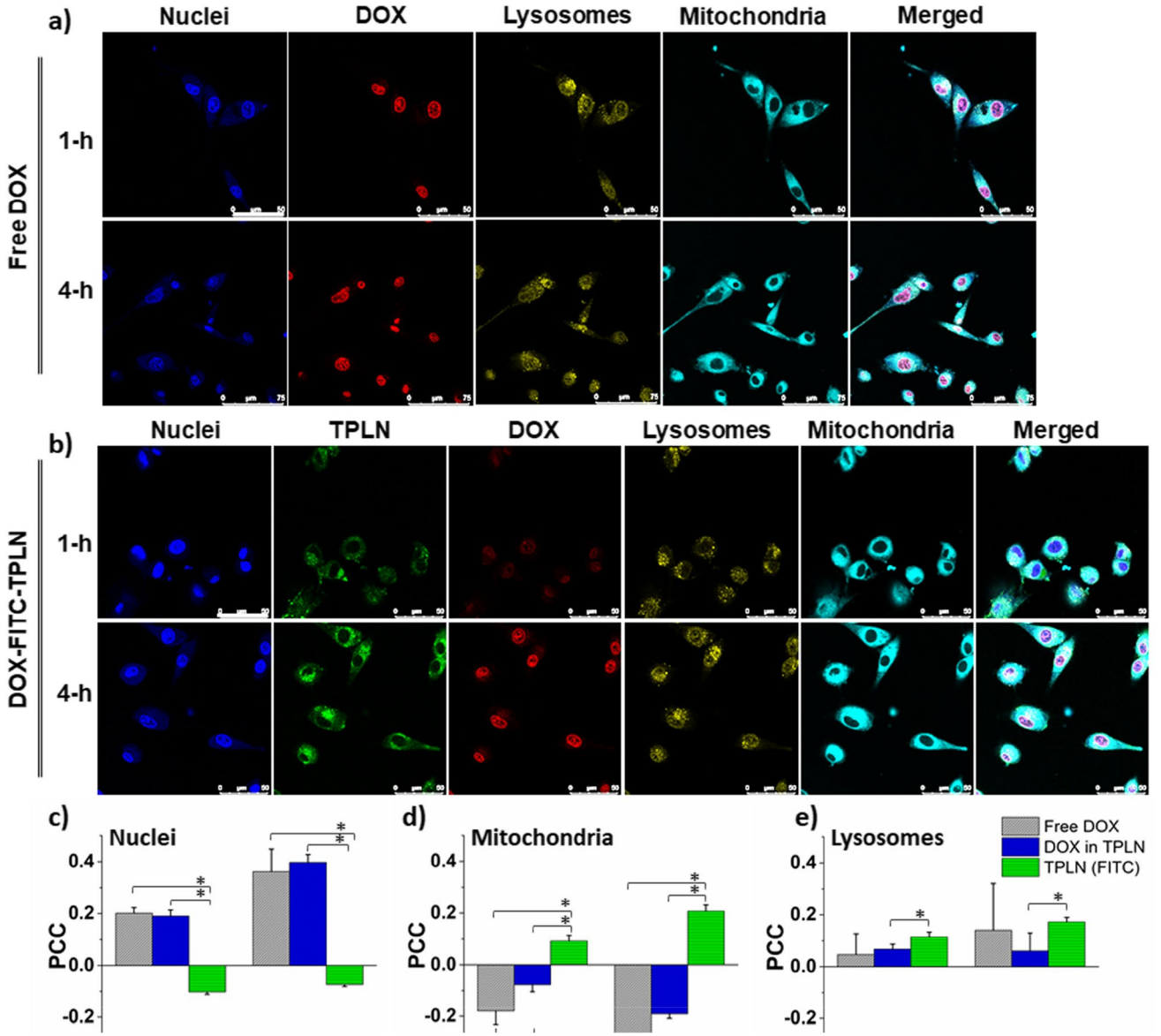

Fig. 5 Confocal microscopic images of ***in vitro*** cellular uptake of free DOX (**a**) and DOX- FITC-TPLN (**b**) in U87-MG-RED-FLuc cells at 1 and 4 h of incubation. The nuclei stained using DAPI (blue), FITC-labeled TPLN (green), DOX (red), lysosomes stained using Lysotracker (orange), mitochondria using Mitotracker (cyan). The scale bar corresponds to 50 μm. **c-e)** Co-localization analyses of confocal images of treated U87-MG-RED-FLuc cells. Correlations of signals between FITC-labeled TPLN or DOX with nuclei (**c**), mitochondria (**d**) and lysosome (**e**) are compared. Standard errors are shown by error bars.

which TPLN were used to delineate the mechanism of cellular uptake in breast cancer cells (36, 69).

In contrast, co-incubation with hRAP, an LDL-R antagonist, showed a significant decrease in uptake compared to incubation with LDL-containing human serum EMEM growth media ($p = 0.0496$) (Fig. 4f). This trend appears consistent with other studies using PS 80-containing NP systems in which LDL-R is purportedly a major endocytotic pathways allowing substance translocation across the BBB (23, 70). U87 GBM cells are known to express LDL-R (71). The ability of TPLN to cross the BBB via LDL-R mediated transcytosis makes it an effective drug carrier to target GBM as well.

Cellular Uptake and Intracellular Fate of DOX-TPLNs

Figure 5 demonstrates the *in vitro* cellular uptake of free DOX and DOX-TPLNs at different times. As shown in the Fig. 5, cellular uptake of free DOX increased from 1 to 4 h in the nuclear compartment (Fig. 5a and c). The PCC between free DOX and nuclei increased

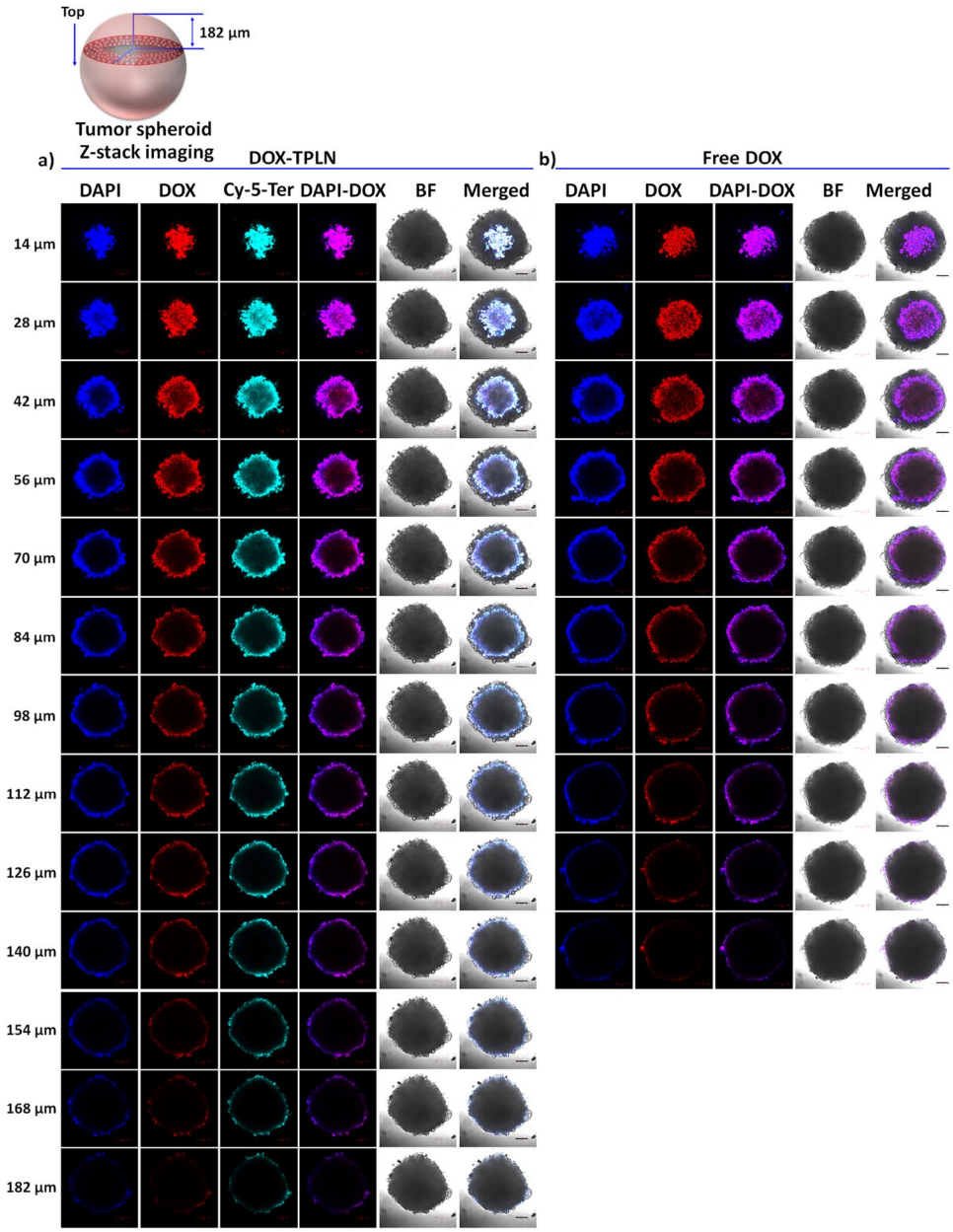

Fig. 6 LSCM images of cross-sections of U87-MG-RED-FLuc tumor spheroids treated with (**a**) DOX-Cy-5-TPLNs or (**b**) free DOX for 4 h. The schematic diagram illustrates the optical slices obtained at every 7 µm starting from the uppermost regions of the spheroids (top). Z-stack LSCM images represent optical sections of spheroids at different depths in the axial direction. After having been fixed with 4% paraformaldehyde, the spheroids were stained with DAPI (blue),and imaged at various wave lengths for nuclei (blue), DOX (red), and Cy-5 labeled-terpolymer TPLN (cyan). Scale bar corresponds to 100 µm for all images. Cy-5 Ter: Cy-5 labeled-terpolymer; BF: Bright field.

(Fig. 5c) with the incubation time but remained the same between DOX and lysosomes (PCC<0.15, Fig. 5e).

Similar to free DOX, DOX-TPLN was greater in the nuclear compartment compared to the mitochondria (Fig. 5 b, c and d). PCC analysis of DOX-TPLNs demonstrated enhanced accumulation of DOX into the nuclei (Fig. 5c) and a slight anti-correlation to mitochondria (PCC<-0.2) (Fig. 5d). Thus, the superior cytotoxicity of DOX-TPLNs (Fig. 3d) might be attributed to the effective cellular uptake of TPLNs and distribution of DOX in intracellular targets over time. Additionally, DOX is a substrate of multiple efflux transporters overexpressed in MDR cancer cells and endothelium at the BBB, therefore, free DOX was not able to induce similar cytotoxicity as compared to the TPLNs. In our recent study, we have reported that DOX-PLNs can exploit different lipid-trafficking pathways to facilitate intracellular organelle specific distribution of DOX (36).

The FITC-labelled TPLNs show an increasing trend in lysosomal uptake from 1 to 4 h (Fig. 5b and e); this indicates that, after sufficient incubation periods, endocytosed TPLNs are released into the cytoplasm, which further supports observations reported in Fig. 4e. TPLNs also showed enhanced co-localization with mitochondria (Fig. 5d), which indicates that components of TPLNs (terpolymer) remained mostly in the cytoplasm (mitochondria and perinuclear area) and delivered loaded cargo to intracellular targets (nuclei). The

overall PCC values for FITC-TPLN with lysosomes and mitochondria were below 0.2 (Fig. 5 d and e).

In vitro Penetration Study of TPLNs on 3D Spheroids

3D tumor spheroids provide an alternative to *in vivo* tumor models and are increasingly utilized to evaluate drug delivery efficiency of NPs (72). This is partly due to the fact that *in vivo* tumor models are costly to establish and partly because they contain variable tumor morphology; making intra-tumoral penetration studies of NPs difficult. For the rational design of TPLNs, 3D spheroids provide an alternative way to evaluate the effectiveness of TPLN at an early stage of the drug development process. Thus, we have chosen a human GBM 3D *in vitro* spheroid tumor model which exhibits the features of solid tumors including 3D spatial arrangement, cell to cell contact, the presence of proliferative gradients, hypoxic gradients, and a necrotic core (72).

The uptake of free DOX and DOX-Cy5-TPLNs was evaluated in U87-MG-RED-FLuc tumor spheroids. Spheroids were incubated for 4 h with treatments and then imaged by LSCM using the z-stack feature (Fig. 6). TPLNs showed deeper penetration of DOX into spheroids in the spheroid periphery and core (Fig. 6a) as compared to the free DOX (Fig. 6b). The distribution of DOX into the nuclear compartment was similar for both treatment groups indicating that TPLNs did not alter the intracellular fate of DOX (Fig. 6 a and b, DAPI-DOX panels). This is significant because spheroid cores of larger spheroids can be hypoxic and have necrotic centers with higher interstitial fluid pressures which reduce the penetration of therapeutics. Peripheral cells of the spheroids assist in growth and extravasation. Thus, the accumulation of TPLNs in the peripheral cells of spheroids further suggests an additional benefit in inhibition of spheroid growth.

In Vivo Biodistribution of TPLNs

A primary brain tumor model was established by stereotactic intracranial injection of U87-MG-RED-FLuc cells into the brains of NRG mice to evaluate the biodistribution of TPLNs. Accumulation of HF 750 labeled DOX-TPLN at the brain tumor site is highlighted by the co-localization of fluorescence from DOX-TPLN with the bioluminescence of brain tumor cells *in vivo* (Fig. 7 a, b). TPLN remained at the tumor site for at least 4 h following treatment. Immediate *ex vivo* fluorescence and bioluminescence imaging of dissected brains at 4 h following DOX-TPLN injection confirmed these results (Fig. 7c). Whole-body bio-distribution imaging demonstrated co-localization of HF 750-labeled TPLNs fluorescence with the tumor bioluminescence area *in vivo*. These results were further supported by the *ex*

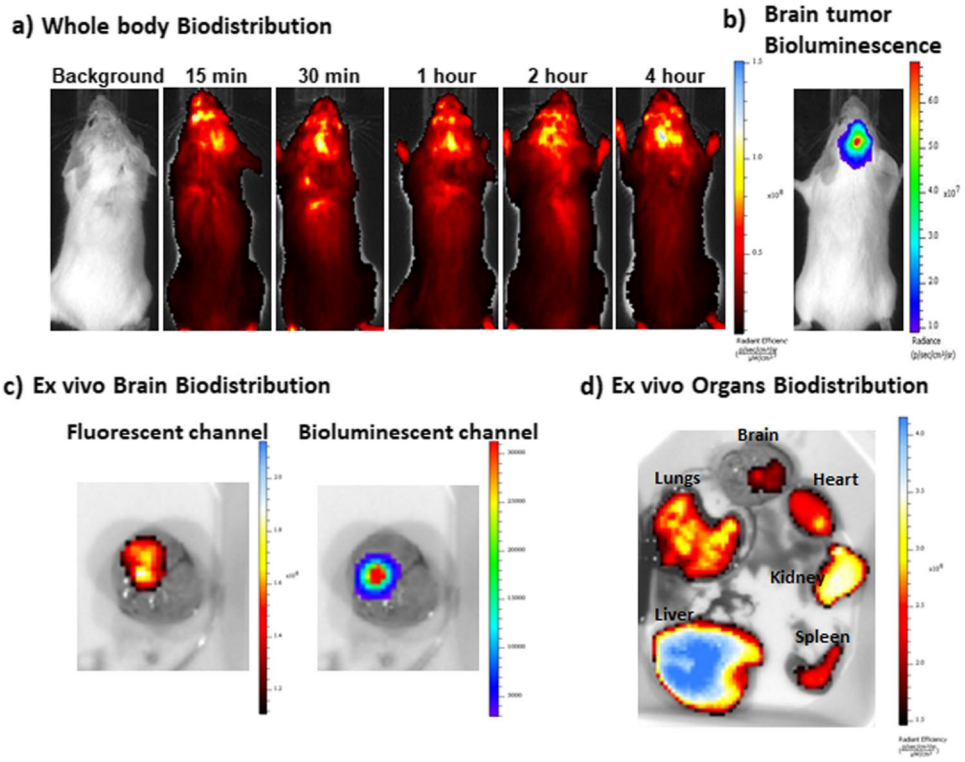

Fig. 7 **a–d)** Whole body *in vivo* images of mice with brain tumor at various times post I.V. injection of TPLN together with *ex vivo* images of organs. The tumor growth and bio-distribution of HF-750 labelled-TPLNs were monitored as a function of luciferin-induced bioluminescence imaging in live animals using a Xenogen IVIS Imaging system. **a)** *In vivo* whole body biodistribution of HF 750-labeled TPLNs in an NRG mouse bearing human glioblastoma U87-MG-RED-FLuc brain tumor . **b)** Brain tumor bioluminescence of tumor in mice taken at 4 h. **c)** *Ex vivo* images of NIR labeled-TPLN in brain tumor (left image: HF 750 filter, right image: bioluminescence signals of brain tumor region). **d)** *Ex vivo* organ bio-distribution of TPLNs. *Ex vivo* images were taken after 4 h.

vivo imaging of the brain (Fig. 7c). Additionally, TPLN accumulated in the major organs following a single I.V. injection of HF 750-labeled DOX-TPLN as determined by *ex vivo* fluorescence imaging (Fig. 7d). Higher fluorescence intensity in the liver and kidneys suggests possible elimination of TPLNs or the HF-750-conjugated polymer through these organs (6, 28). The biodistribution studies are consistent with our previous findings in which TPLNs showed enhanced accumulation in the brain and also showed higher accumulation in the liver and kidneys (6, 28). The enhanced fluorescent signal of HF 750 in kidney is ascribed to the renal clearance of dye labeled polymers (28). Likewise, the higher signal in the liver indicates the TPLNs are probably undergoing liver metabolism.

CONCLUSION

A GBM and BBB-permeable TPLN formulation was devised to deliver the brain-impermeable anticancer drug DOX for the treatment of GBM. The composition of lipid in combination with the BBB-crossing terpolymer was optimized using the 2^3 factorial experimental design to achieve optimal NP properties and maximum anticancer efficacy for ultimate intravenous administration to target GBM. Of various investigated lipid candidates, EA enabled the formation of DOX-TPLNs with desirable colloidal properties and stability, and the highest potency against U87 GBM cells. The optimized TPLNs showed enhanced cellular uptake compared to free DOX, without reducing nuclear accumulation of DOX. *In vitro* inhibition studies suggested that TPLNs enter GBM cells via clathrin-dependent endocytosis and phagocytosis mechanisms. The interaction of TPLN with LDL-R facilitated cellular uptake by GBM cells, penetration through the 3D spheroids, and BBB-crossing to orthotopic GBM in an experimental brain tumor model, likely via LDL-R-mediated transcytosis. Confocal microscopy revealed that the DOX-TPLN enhanced nuclear uptake of DOX. The results of this work suggest that lipid composition and content in a PLN system play important roles and can be optimized to achieve superior *in vitro* and *in vivo* performances.

ACKNOWLEDGMENTS AND DISCLOSURES

The authors would like to thank the Canadian Institutes of Health Research (CIHR) for an Operating Grant to X.Y.W, A.M.R. and J.T.H and the Natural Sciences and Engineering Research Council (NSERC) of Canada for equipment grants to X.Y.W; Connaught International Scholarship for Doctoral students and top up scholarship from the Graduate Department of Pharmaceutical Sciences, University of Toronto to T.A.

The authors declare no competing financial interest.

AUTHOR CONTRIBUTIONS X.Y.W. conceived the project. T.A., and F–C F.L. designed and conducted the experiments, performed the analysis and interpretations, and wrote the paper. T.A., C.H, P.C. and A.Z.A performed the bio-distribution experiments. A.M.R., J.T.H, and X.Y.W. conceived the hypotheses, designed the experiments, and edited the paper. The manuscript has been revised and read by all authors.

REFERENCES

1. Karim R, Palazzo C, Evrard B, Piel G. Nanocarriers for the treatment of glioblastoma multiforme: Current state-of-the-art. J Control Release. 2016;227:23–37.
2. Saraiva C, Praca C, Ferreira R, Santos T, Ferreira L, Bernardino L. Nanoparticle-mediated brain drug delivery: Overcoming blood-brain barrier to treat neurodegenerative diseases. J Control Release. 2016;235:34–47.
3. Wong HL, Wu XY, Bendayan R. Nanotechnological advances for the delivery of CNS therapeutics. Adv Drug Deliv Rev. 2012;64(7):686–700.
4. Terstappen GC, Meyer AH, Bell RD, Zhang W. Strategies for delivering therapeutics across the blood-brain barrier. Nat Rev Drug Discov. 2021;20(5):362–83.
5. Deeken JF, Loscher W. The blood-brain barrier and cancer: transporters, treatment, and Trojan horses. Clin Cancer Res. 2007;13(6):1663–74.
6. Li J, Cai P, Shalviri A, Henderson JT, He C, Foltz WD, Prasad P, Brodersen PM, Chen Y, DaCosta R, Rauth AM, Wu XY. A multifunctional polymeric nanotheranostic system delivers doxorubicin and imaging agents across the blood-brain barrier targeting brain metastases of breast cancer. ACS Nano. 2014;8(10):9925–40.
7. Lee CY. Strategies of temozolomide in future glioblastoma treatment. Onco Targets Ther. 2017;10:265–70.
8. Lee SY. Temozolomide resistance in glioblastoma multiforme. Genes & Diseases. 2016;3(3):198–210.
9. Chamberlain MC. Temozolomide: therapeutic limitations in the treatment of adult high-grade gliomas. Expert Rev Neurother. 2010;10(10):1537–44.
10. Kim SS, Rait A, Kim E, Pirollo KF, Chang EH. A tumor-targeting p53 nanodelivery system limits chemoresistance to temozolomide prolonging survival in a mouse model of glioblastoma multiforme. Nanomedicine. 2015;11(2):301–11.
11. Han J, Jun Y, Kim SH, Hoang HH, Jung Y, Kim S, Kim J, Austin RH, Lee S, Park S. Rapid emergence and mechanisms of resistance by U87 glioblastoma cells to doxorubicin in an in vitro tumor microfluidic ecology. Proc Natl Acad Sci U S A. 2016;113(50):14283–8.
12. Genomics of Drug Sensitivity in Cancer, https://www.cancerrxgene.org/compound/Doxorubicin/133/overview/ic50, Accessed on August 14, 2021.
13. Pinzon-Daza M, Garzon R, Couraud P, Romero I, Weksler B, Ghigo D, Bosia A, Riganti C. The association of statins plus LDL receptor-targeted liposome-encapsulated doxorubicin increases in vitro drug delivery across blood-brain barrier cells. Br J Pharmacol. 2012;167(7):1431–47.
14. Dong X. Current strategies for brain drug delivery. Theranostics. 2018;8(6):1481–93.

15. Jena L, McErlean E, McCarthy H. Delivery across the blood-brain barrier: nanomedicine for glioblastoma multiforme. Drug Deliv Transl Res. 2020;10(2):304–18.
16. Reddy S, Tatiparti K, Sau S, Iyer AK. Recent advances in nano delivery systems for blood-brain barrier (BBB) penetration and targeting of brain tumors. Drug Discov Today. 2021.
17. Pandit R, Chen L, Götz J. The blood-brain barrier: Physiology and strategies for drug delivery. Adv Drug Deliv Rev. 2020;165–166:1–14.
18. Kreuter J. Nanoparticulate systems for brain delivery of drugs. Adv Drug Del Rev. 2012;64(SUPPL.):213–222.
19. Wohlfart S, Gelperina S, Kreuter J. Transport of drugs across the blood-brain barrier by nanoparticles. J Control Release. 2012;161(2):264–73.
20. Kreuter J. Mechanism of polymeric nanoparticle-based drug transport across the blood-brain barrier (BBB). J Microencapsul. 2013;30(1):49–54.
21. Kreuter J. Drug delivery to the central nervous system by polymeric nanoparticles: what do we know? Adv Drug Deliv Rev. 2014;71:2–14.
22. Wohlfart S, Khalansky AS, Bernreuther C, Michaelis M, Cinatl J Jr, Glatzel M, Kreuter J. Treatment of glioblastoma with poly(isohexyl cyanoacrylate) nanoparticles. Int J Pharm. 2011;415(1–2):244–51.
23. He C, Ahmed T, Abbasi AZ, Li LY, Foltz WD, Cai P, Knock E, Fraser PE, Rauth AM, Henderson JT, Wu XY. Multifunctional bioreactive-nanoconstructs for sensitive and accurate MRI of cerebrospinal fluid pathology and intervention of Alzheimer's disease. Nano Today. 2020;35:100965.
24. Olivier J-C, Fenart L, Chauvet R, Pariat C, Cecchelli R, Couet W. Indirect evidence that drug brain targeting using polysorbate 80-coated Polybutylcyanoacrylate nanoparticles is related to toxicity. Pharm Res. 1999;16(12):1836–42.
25. Olivier J-C. Drug transport to brain with targeted nanoparticles. NeuroRx. 2005;2(1):108–19.
26. He C, Cai P, Li J, Zhang T, Lin L, Abbasi AZ, Henderson JT, Rauth AM, Wu XY. Blood-brain barrier-penetrating amphiphilic polymer nanoparticles deliver docetaxel for the treatment of brain metastases of triple negative breast cancer. J Control Release. 2017;246:98–109.
27. Shalviri A, Cai P, Rauth AM, Henderson JT, Wu XY. Evaluation of new bi-functional terpolymeric nanoparticles for simultaneous in vivo optical imaging and chemotherapy of breast cancer. Drug Deliv Transl Res. 2012;2(6):437–53.
28. Zhang T, Lip H, He C, Cai P, Wang Z, Henderson JT, Rauth AM, Wu XY. Multitargeted nanoparticles deliver synergistic drugs across the blood-brain barrier to brain metastases of triple negative breast cancer cells and tumor-associated macrophages. Adv Healthc Mater. 2019;8(18):e1900543.
29. He C, Li J, Cai P, Ahmed T, Henderson JT, Foltz WD, Bendayan R, Rauth AM, Wu XY. Two-step targeted hybrid nanoconstructs increase brain penetration and efficacy of the therapeutic antibody trastuzumab against brain metastasis of HER2-positive breast cancer. Adv Funct Mater. 2018;28(9):1705668.
30. Zhang RX, Ahmed T, Li LY, Li J, Abbasi AZ, Wu XY. Design of nanocarriers for nanoscale drug delivery to enhance cancer treatment using hybrid polymer and lipid building blocks. Nanoscale. 2017;9(4):1334–55.
31. Wu XY. Strategies for optimizing polymer-lipid hybrid nanoparticle-mediated drug delivery. Expert Opin Drug Deliv. 2016;13(5):609–12.
32. Park JH, Ban SJ, Ahmed T, Choi HS, Yoon HE, Yoon JH, Choi HK. Development of DH-I-180-3 loaded lipid nanoparticle for photodynamic therapy. Int J Pharm. 2015;491(1–2):393–401.
33. Li Y, Taulier N, Rauth AM, Wu XY. Screening of lipid carriers and characterization of drug-polymer-lipid interactions for the rational design of polymer-lipid hybrid nanoparticles (PLN). Pharm Res. 2006;23(8):1877–87.
34. Wong HL, Rauth AM, Bendayan R, Manias JL, Ramaswamy M, Liu Z, Erhan SZ, Wu XY. A new polymer-lipid hybrid nanoparticle system increases cytotoxicity of doxorubicin against multidrug-resistant human breast cancer cells. Pharm Res. 2006;23(7):1574–85.
35. Li Y, Wong HL, Shuhendler AJ, Rauth AM, Wu XY. Molecular interactions, internal structure and drug release kinetics of rationally developed polymer-lipid hybrid nanoparticles. J Control Release. 2008;128(1):60–70.
36. Amini MA, Ahmed T, Liu FF, Abbasi AZ, Soeandy CD, Zhang RX, Prashad P, Cummins CL, Rauth AM, Henderson JT, Wu XY. Exploring the transformability of polymer-lipid hybrid nanoparticles and nanomaterial-biology interplay to facilitate tumor penetration, cellular uptake and intracellular targeting of anticancer drugs. Expert Opin Drug Deliv. 2021:1–14.
37. Omer ME, Halwani M, Alenazi RM, Alharbi O, Aljihani S, Massadeh S, Al Ghoribi M, Al Aamery M, Yassin AE. Novel self-assembled polycaprolactone-lipid hybrid nanoparticles enhance the antibacterial activity of ciprofloxacin. SLAS Technol. 2020;25(6):598–607.
38. Azandaryani AH, Kashanian S, Shahlaei M, Derakhshandeh K, Motiei M, Moradi S. A comprehensive physicochemical, in vitro and molecular characterization of letrozole incorporated chitosan-lipid nanocomplex. Pharm Res. 2019;36(4):62.
39. Pokharkar VB, Jolly MR, Kumbhar DD. Engineering of a hybrid polymer-lipid nanocarrier for the nasal delivery of tenofovir disoproxil fumarate: physicochemical, molecular, microstructural, and stability evaluation. Eur J Pharm Sci. 2015;71:99–111.
40. Shuhendler AJ, Cheung RY, Manias J, Connor A, Rauth AM, Wu XY. A novel doxorubicin-mitomycin C co-encapsulated nanoparticle formulation exhibits anti-cancer synergy in multidrug resistant human breast cancer cells. Breast Cancer Res Treat. 2010;119(2):255–69.
41. Li Y, Abbaspour MR, Grootendorst PV, Rauth AM, Wu XY. Optimization of controlled release nanoparticle formulation of verapamil hydrochloride using artificial neural networks with genetic algorithm and response surface methodology. Eur J Pharm Biopharm. 2015;94:170–9.
42. Yuangyai C, Nembhard HB. Chapter 8 - Design of Experiments: A Key to Innovation in Nanotechnology. In: Ahmed W, Jackson MJ, editors. Emerging Nanotechnologies for Manufacturing. Boston: William Andrew Publishing; 2010. p. 207–34.
43. Yu LX. Pharmaceutical quality by design: product and process development, understanding, and control. Pharm Res. 2008;25(4):781–91.
44. Shah B, Khunt D, Bhatt H, Misra M, Padh H. Application of quality by design approach for intranasal delivery of rivastigmine loaded solid lipid nanoparticles: Effect on formulation and characterization parameters. Eur J Pharm Sci. 2015;78:54–66.
45. Zhang J, Fan Y, Smith E. Experimental design for the optimization of lipid nanoparticles. J Pharm Sci. 2009;98(5):1813–9.
46. Jo DH, Kim JH, Lee TG, Kim JH. Size, surface charge, and shape determine therapeutic effects of nanoparticles on brain and retinal diseases. Nanomedicine. 2015;11(7):1603–11.

47. Duan X, Li Y. Physicochemical characteristics of nanoparticles affect circulation, biodistribution, cellular internalization, and trafficking. Small. 2013;9(9–10):1521–32.
48. ShindePatil VR, Campbell CJ, Yun YH, Slack SM, Goetz DJ. Particle diameter influences adhesion under flow. Biophys J. 2001;80(4):1733–43.
49. Yoo J-W, Irvine DJ, Discher DE, Mitragotri S. Bio-inspired, bioengineered and biomimetic drug delivery carriers. Nat Rev Drug Discov. 2011;10(7):521–35.
50. Frosina G. Nanoparticle-mediated drug delivery to high-grade gliomas. Nanomedicine. 2016;12(4):1083–93.
51. Anselmo AC, Mitragotri S. Impact of particle elasticity on particle-based drug delivery systems. Adv Drug Deliv Rev. 2016.
52. Yoo JW, Doshi N, Mitragotri S. Adaptive micro and nanoparticles: temporal control over carrier properties to facilitate drug delivery. Adv Drug Deliv Rev. 2011;63(14–15):1247–56.
53. Jiang W, Kim BY, Rutka JT, Chan WC. Nanoparticle-mediated cellular response is size-dependent. Nat Nanotechnol. 2008;3(3):145–50.
54. Yoo JW, Mitragotri S. Polymer particles that switch shape in response to a stimulus. Proc Natl Acad Sci U S A. 2010;107(25):11205–10.
55. Danaei M, Dehghankhold M, Ataei S, Hasanzadeh Davarani F, Javanmard R, Dokhani A, Khorasani S, Mozafari MR. Impact of particle size and polydispersity index on the clinical applications of lipidic nanocarrier systems. Pharmaceutics. 2018;10(2):57.
56. Zhang RX, Cai P, Zhang T, Chen K, Li J, Cheng J, Pang KS, Adissu HA, Rauth AM, Wu XY. Polymer-lipid hybrid nanoparticles synchronize pharmacokinetics of co-encapsulated doxorubicin-mitomycin C and enable their spatiotemporal co-delivery and local bioavailability in breast tumor. Nanomedicine. 2016;12(5):1279–90.
57. Cheng D, Cao N, Chen J, Yu X, Shuai X. Multifunctional nanocarrier mediated co-delivery of doxorubicin and siRNA for synergistic enhancement of glioma apoptosis in rat. Biomaterials. 2012;33(4):1170–9.
58. Battaglia L, Gallarate M, Peira E, Chirio D, Muntoni E, Biasibetti E, Capucchio MT, Valazza A, Panciani PP, Lanotte M, Schiffer D, Annovazzi L, Caldera V, Mellai M, Riganti C. Solid lipid nanoparticles for potential doxorubicin delivery in glioblastoma treatment: preliminary in vitro studies. J Pharm Sci. 2014;103(7):2157–65.
59. Subedi RK, Kang KW, Choi HK. Preparation and characterization of solid lipid nanoparticles loaded with doxorubicin. Eur J Pharm Sci. 2009;37(3–4):508–13.
60. Kang KW, Chun MK, Kim O, Subedi RK, Ahn SG, Yoon JH, Choi HK. Doxorubicin-loaded solid lipid nanoparticles to overcome multidrug resistance in cancer therapy. Nanomedicine. 2010;6(2):210–3.
61. Shalviri A, Raval G, Prasad P, Chan C, Liu Q, Heerklotz H, Rauth AM, Wu XY. pH-Dependent doxorubicin release from terpolymer of starch, polymethacrylic acid and polysorbate 80 nanoparticles for overcoming multi-drug resistance in human breast cancer cells. Eur J Pharm Biopharm. 2012;82(3):587–97.
62. Tapeinos C, Battaglini M, Ciofani G. Advances in the design of solid lipid nanoparticles and nanostructured lipid carriers for targeting brain diseases. J Control Release. 2017;264:306–32.
63. Patil GB, Surana SJ. Bio-fabrication and statistical optimization of polysorbate 80 coated chitosan nanoparticles of tapentadol hydrochloride for central antinociceptive effect: in vitro-in vivo studies. Artificial cells, nanomedicine, and biotechnology. 2017;45(3):505–14.
64. Freitas C, Müller RH. Effect of light and temperature on zeta potential and physical stability in solid lipid nanoparticle (SLN^{TM}) dispersions. Int J Pharm. 1998;168(2):221–9.
65. Mehnert W, Mäder K. Solid lipid nanoparticles: production, characterization and applications. Adv Drug Deliv Rev. 2001;47(2–3):165–96.
66. Zou Y, Liu Y, Yang Z, Zhang D, Lu Y, Zheng M, Xue X, Geng J, Chung R, Shi B. Effective and Targeted Human Orthotopic Glioblastoma Xenograft Therapy via a Multifunctional Biomimetic Nanomedicine. Adv Mater. 2018;30(51):e1803717.
67. Ahmed T, Kamel AO, Wettig SD. Interactions between DNA and Gemini surfactant: impact on gene therapy: part I. Nanomedicine (Lond). 2016;11(3):289–306.
68. Ahmed T, Kamel AO, Wettig SD. Interactions between DNA and gemini surfactant: impact on gene therapy: part II. Nanomedicine (Lond). 2016;11(4):403–20.
69. Wang Z, Zhang RX, Zhang T, He C, He R, Ju X, Wu XY. In situ proapoptotic peptide-generating rapeseed protein-based nanocomplexes synergize chemotherapy for cathepsin-b overexpressing breast cancer. ACS Appl Mater Interfaces. 2018;10(48):41056–69.
70. Gelperina S, Maksimenko O, Khalansky A, Vanchugova L, Shipulo E, Abbasova K, Berdiev R, Wohlfart S, Chepurnova N, Kreuter J. Drug delivery to the brain using surfactant-coated poly(lactide-co-glycolide) nanoparticles: influence of the formulation parameters. Eur J Pharm Biopharm. 2010;74(2):157–63.
71. Bu G, Maksymovitch EA, Geuze H, Schwartz AL. Subcellular localization and endocytic function of low density lipoprotein receptor-related protein in human glioblastoma cells. J Biol Chem. 1994;269(47):29874–82.
72. Nunes AS, Barros AS, Costa EC, Moreira AF, Correia IJ. 3D tumor spheroids as in vitro models to mimic in vivo human solid tumors resistance to therapeutic drugs. Biotechnol Bioeng. 2019;116(1):206–26.

Publisher's Note Springer Nature remains neutral with regard to jurisdictional claims in published maps and institutional affiliations.